Nuclear Physics B144 (1978) 22–60

ELASTIC AND INELASTIC ϕ PHOTOPRODUCTION

H.-J. BEHREND, J. BODENKAMP, W.P. HESSE *, W.A. McNEELY Jr., ** and T. MIYACHI ***
Deutsches Elektronen-Synchrotron, DESY, Hamburg

D.C. FRIES, P. HEINE +, H. HIRSCHMANN ++, A. MARKOU and E. SEITZ
Institut für Kernphysik des Kernforschungszentrum
and
Institut für Experimentelle Kernphysik der Universität Karlsruhe

Received 5 June 1978

The differential cross section of the reaction ($\gamma p \to p\phi$) has been measured in the t range $0 \leqslant t \leqslant 0.4$ GeV^2 and for photon energies from 3.0 to 6.7 GeV. In particular for the small t region the measurement accuracy was better than 10%. We obtained for the slope parameter B in an exponential parametrization of the differential cross section $d\sigma/dt = Ae^{-Bt}$ values of $B \simeq 6 \pm 0.5$ GeV^{-2} which are significantly larger than the slopes obtained by most other experiments at higher t values. This indicates a t dependence of B particularly in the small t region.

An energy dependence of the optical point $(d\sigma/dt)_{t=0}$, observed in our measurements, has been explained as a kinematic effect due to the VDM relation. A fit of our measurements is in excellent agreement with all other published values of $(d\sigma/dt)_{t=0}(\gamma p \to \phi p)$, this implies that $\sigma_{tot}(\phi p)$ must be essentially energy independent in this energy range.

Spin density matrix elements of the ϕ have been evaluated and an analysis of the helicity amplitudes has been carried out. This analysis confirmed s-channel helicity conservation. Moments of spherical harmonics of the $K\bar{K}$ angular decay distribution have been computed for 10 MeV $K\bar{K}$ mass-bins from threshold to 1.3 GeV. The mass dependence of the normalized moments is generally smooth. Contributing amplitudes have essentially only even moments. The moment $\langle Y_2^0 \rangle / \langle Y_0^0 \rangle$ changes sign above the ϕ mass.

Differential cross sections for the inelastic ϕ production $\gamma p \to \phi X$ have been evaluated for the first time both with respect to $t - t_{min}$ and M_X. The integrated inelastic cross sections are comparable in size with the elastic ones. The slopes of the differential cross sections $d\sigma/dt$ appear to become flatter with increasing M_X.

* Now: Department of Physics, Randolph-Macon College, Ashland, Va. 23005, USA.
** Now: Boeing Computer Services, Seattle, Washington 91868, USA.
*** Now: Institute for Nuclear Study, University of Tokyo, Tanashi, Tokyo 188, Japan.
+ Now: II. Institut für Experimentalphysik der Universität Hamburg, Luruper Chaussee 149, D-2000 Hamburg 52.
++ Now: SIN, Swiss Institute for Nuclear Research, CH-5234 Villingen.

1. Introduction

In this paper [1] results are presented which were obtained from the measurement and analysis of photoproduced K^+K^- final states with an invariant mass near the phi-meson mass (1020 MeV). The data have been taken in a high statistics experiment performed at DESY using a tagged-photon beam, a forward wire-chamber magnetic spectrometer and a threshold Čerenkov counter. The analysis was essentially concerned with two reaction channels

$$\gamma p \to \phi p \to K^+K^- p \,, \tag{1.1}$$

which will be called the 'elastic ϕ photoproduction' (in the spirit of the vector-meson dominance picture), and

$$\gamma p \to \phi X \to K^+K^- X \; (X \neq p) \,, \tag{1.2}$$

which will be referred to as 'inelastic ϕ photoproduction'.

Reaction (1.1) has been studied for photon energies E_γ in the range from 3.0 to 6.7 GeV, reaction (1.2) in the energy range $4.6 \leqslant E_\gamma \leqslant 6.7$ GeV. In reaction (1.2) the missing mass lies in the interval $1.20 \leqslant M_X \leqslant 2.1$ GeV.

Phi photoproduction has been measured previously in a number of experiments up to photon energies of about 20 GeV [2], using mostly a Bremsstrahlung photon beam. This experiment has several distinguishing features in comparison with other phi-meson photoproduction experiments: (i) it is the first high-statistics experiment to systematically analyse the small t-region $|t| < 0.4$ GeV^2; (ii) the measurement of the incident photon energy and the possibility to reconstruct the kinematic of an elastic event assured the separation of elastic and inelastic events.

2. Theoretical interest in ϕ photoproduction

The interest in the photoproduction of the ϕ meson is closely connected to two rather fundamental theoretical problems in particle physics: the photon-hadron coupling and the diffractive scattering of hadrons.

Firstly, the phi is a neutral isoscalar meson resonance at a mass of 1020 MeV with spin, parity and charge conjugation identical to the photon, namely, $J^{PC} = 1^{--}$. Due to the similarity of the ϕ and γ quantum numbers, the ϕ (as well as the other vector mesons) plays an important role in photon physics for photon energies greater than a few GeV.

The vector-meson dominance model (VDM) describes an equivalence between the amplitude f_γ of the photon induced reaction $\gamma + B \to V + B$, and that caused by a transversely polarized vector meson ($V' + B \to V + B$), namely,

$$f_\gamma(\gamma B \to VB) = \sum_{V'} \sqrt{\frac{\alpha}{4}\frac{4\pi}{\gamma_V^2}} f_V(V'B \to VB) \,, \tag{2.1}$$

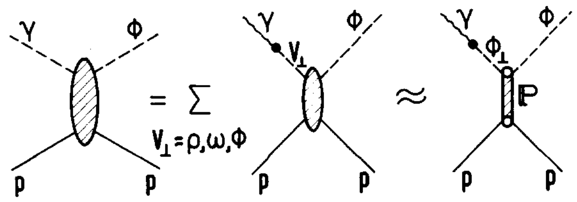

Fig. 1. The production mechanism of the ϕ meson based on the vector meson dominance model The elastic ϕ is produced by the exchange of a single pomeron trajectory.

where α is the fine-structure constant, $\gamma_V^2/4\pi$ is the γV coupling constant and V$'$ represents the transverse part of the vector mesons ρ, ω, ϕ (because of the energy domain discussed, contributions of the ψ family can be neglected) and B the target nucleon. So that for the case of ϕ photoproduction on protons the amplitude from eq. (2.1) is of the following form:

$$f_\gamma(\gamma + \mathrm{p} \to \phi + \mathrm{p}) = \sqrt{\frac{\alpha}{4}\frac{4\pi}{\gamma_\phi^2}}\, f_\phi(\phi' + \mathrm{p} \to \phi + \mathrm{p})\,, \tag{2.2}$$

where contributions from mixed terms (e.g. ρp $\to$ ϕp) are assumed to be negligible. Hence the ϕ photoproduction is related to the hadronic reaction, $\phi' + \mathrm{p} \to \phi + \mathrm{p}$ (fig. 1).

The second point of interest is the SU(3) assignment of the ϕ meson [3]. With the assumption of an ideal singlet octet-mixing, the ϕ is built solely from s and $\bar{\mathrm{s}}$ quarks. This assumption is experimentally supported for example by the measurement of the ratio $\sigma(\pi^-\mathrm{p} \to \phi\mathrm{n})/\sigma(\pi^-\mathrm{p} \to \omega\mathrm{n}) = 0.035 \pm 0.0010$ [4], which is equal to the fraction of non-strange quarks contained in the phi. The Okubo-Zweig-Iizuka rule then predicts that a direct interaction of the ϕ with particle states built only from non-strange quarks is strongly inhibited [4].

Because there are no strange s- and u-channel resonances which could couple to the ϕ, only the t-channel exchanges with CP = ++ and I = 0 (as required by charge conjugation invariance) can contribute, that is only trajectories such as the pomeron, f(1270) and f$'$(1514). However due to its non-strange quark content, the P$'$ trajectory, which is identified with the f(1270), decouples in the t-channel *. Even if one assumes a similar nature for f$'$(1514) as for the ϕ meson, the exchange of the associated trajectory (P$''$) would be suppressed by its low-lying nature **. Thus the elastic ϕp scattering is considered to occur through the exchange of only the pomeron trajectory.

* The f meson decays predominantly into pure pion final states, BR(f $\to 2\pi$/f $\to$ all) = 0.81 ± 0.01, BR(f $\to 4\pi$/f $\to$ all) = 0.028 ± 0.003, BR(f $\to \mathrm{K\bar{K}}$/f $\to$ all) = 0.027 ± 0.006 (see Rosenfeld tables and [5]).

** The decay branching ratio of the f$'$ meson is not accurately known. It will not entirely decouple from $\bar{\mathrm{p}}$p. By considering its mass and spin, the intersecting point of the P$''$ trajectory would be smaller than $\alpha_f(0) = 0.41$ [6].

From eq. (2.2), one obtains the differential cross section for the photoproduction

$$\frac{d\sigma}{dt}(\gamma p \to \phi p) = \frac{\alpha}{4}\frac{4\pi}{\gamma_\phi^2}\left(\frac{p_\phi}{k}\right)^2 \frac{d\sigma}{dt}(\phi p \to \phi p) , \tag{2.3}$$

where p_ϕ is the momentum of the ϕ meson, k is that of the incident photon in the c.m.s. and t is the four-momentum transfer squared. The total cross section of the reaction $\sigma_T(\phi p \to \phi p)$ is obtained by the optical theorem:

$$\left(\frac{d\sigma}{dt}(\gamma p \to \phi p)\right)_{t=0} = \frac{\alpha}{64\pi}\frac{4\pi}{\gamma_\phi^2}(1+\eta_\phi^2)\left(\frac{p_\phi}{k}\right)^2 \sigma_T^2(\phi p \to \phi p) , \tag{2.4}$$

where $(d\sigma/dt)_{t=0}$ is the extrapolated optical point and η_ϕ is the ratio of real to imaginary amplitude at $t = 0$.

In particular the energy dependence of the differential cross section and of the slope parameter can be analyzed applying the Regge model and a simple pole picture for the pomeron trajectory. Although the naive pole picture for the pomeron trajectory is generally untenable, as diffraction scattering data at very high energy have demonstrated, it may, at our energy range, still be a useful parametrization. Thus we parametrize the cross section in terms of a single pole exchange

$$\frac{d\sigma}{dt} = F(t)\left(\frac{s}{s_0}\right)^{2(\alpha(t)-1)} , \tag{2.5}$$

where s is the c.m. energy squared, s_0 is a scale factor customarily set to 1 GeV^2, $\alpha(t)$ is the exchanged trajectory and $F(t)$ represents the square of the residue function. For the pomeron trajectory $\alpha(t)$ is parametrized as $\alpha_p(t) = 1 + \alpha'_p(0)t$ with the slope parameter $\alpha'_p(0)$. The residue function is assumed to be

$$F(t) = A \exp(at + bt^2) , \tag{2.6}$$

where A, a and b are parameters determined by experimental data.

Consequently the differential cross section is described as follows:

$$\frac{d\sigma}{dt} = A \exp(m(s, t)) , \tag{2.7}$$

with

$$m(s, t) = (a + 2\alpha'(0) \ln(s/s_0))\, t + bt^2 . \tag{2.8}$$

An additional insight into the diffractive nature of the ϕ photoproduction can be obtained studying the ϕ decay. The analysis of the decay angular distribution of the $K\bar{K}$ system provides information on the dynamics of the reaction (1.1) by establishing the statistical population of the spin states of the ϕ, with their mass- and their t-dependence. It has been proposed that the s-channel helicity conservation is an essential feature of a diffractive process [7]. Thus, studying the helicity structure of the ϕ production gives some information on the dynamics of pomeron exchange. Pomeron exchange is a model of diffraction scattering on one hand and at the same time a feature of ϕ photoproduction suggested by the quark model.

3. Experimental procedures

3.1. Experimental set up

A schematic drawing of the experimental set up is presented in fig. 2. An electron beam was ejected from the synchrotron with a momentum spread $\Delta p/p = 0.25\%$. The beam was horizontally focussed to a $1 \times 10\ \mathrm{mm}^2$ shape on an aluminium radiator of 1 mm thickness. Downstream of the radiator, a tagging system was placed to analyse the momentum of the deflected electrons. The non-interacting electron beam was absorbed in a quantameter used for overall flux normalization.

While traversing an evacuated beam pipe to a liquid hydrogen target, the photon beam passed through a 20 cm long lead collimator, a pair of beam scrapers each remotely controlled in vertical and horizontal directions, a sweeping magnet and a lead-concrete wall.

At the liquid hydrogen target (50 cm long and 2.5 cm diameter), the photon beam was nearly Gaussian shaped with a half width of 7 mm. The target was surrounded by a hodoscope which consisted of 23 scintillation counters each $3.3 \times 57.5\ \mathrm{cm}^2$ extended parallel to the beam in a cylindrical array of 26 cm diameter. This hodoscope was inside the vacuum tank of the hydrogen target. The light was directed through optical guides to the outside. The target hodoscope detected the recoil protons and measured their azimuthal angles, thus checking the coplanarity condition between recoil proton and reconstructed kaon pair system.

Photons which did not interact in the target, as well as electrons produced in materials along the beam line, passed through a hole in the front trigger counters, traversed four planes of multiwire proportional chambers and hit a 60 cm long lead absorber suspended at the entrance of a large aperture analysing magnet. Hadrons produced at larger angles passed through (i) an array of front trigger counters, (ii) four multiwire proportional chambers, (iii) the large aperture analysing magnet with a field strength of 9.5 kG · m, (iv) a set of eight spark chambers each $1 \times 1\ \mathrm{m}^2$ with magnetic core readout, (v) a double wall of trigger counters and (vi) a gas threshold Čerenkov counter which discriminated against electrons and pions. The specifications of each component are presented in table 1a.

Data have been taken in three periods, each with a different incident electron energy as shown in table 2. For the lower energy runs (Exp. II and III) a different experimental configuration from the one explained above was used to compensate for a reduction of detection efficiency of the spectrometer. The configuration was modified as follows: an array of 16 scintillation counters extending vertically replaced the front trigger counters mentioned above; only the larger multiwire pro-

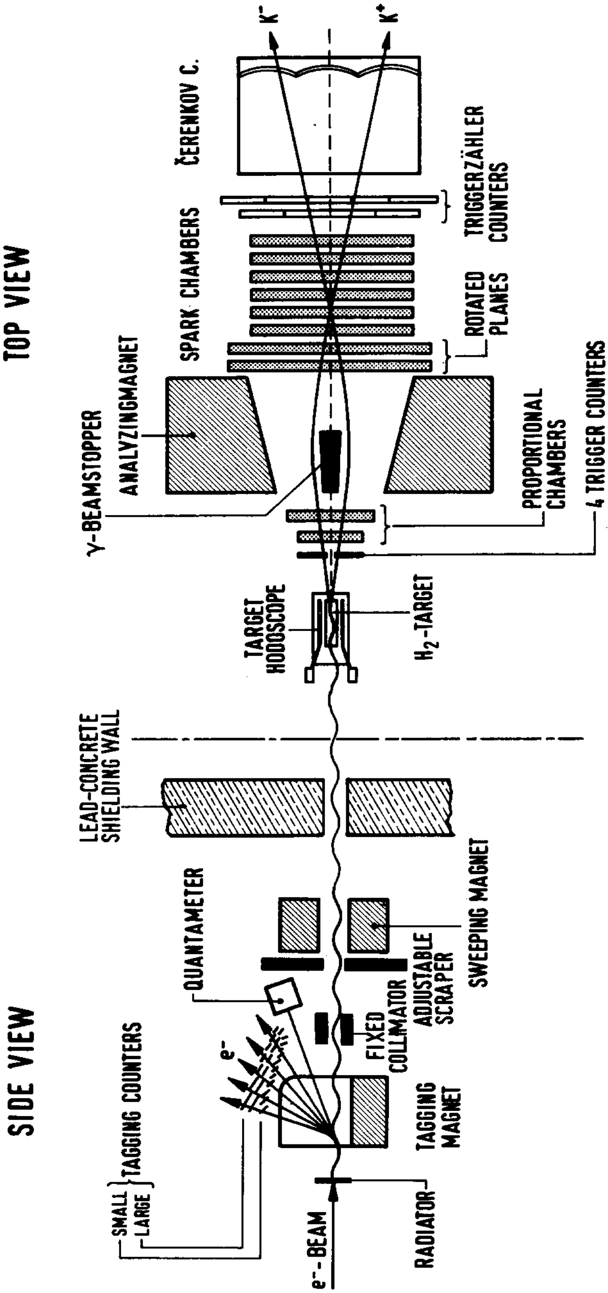

Fig. 2. The experimental set up used for Exp I.

Table 1

A summary of specifications of components used in this experiment, (a) for Exp I, (b) components changed in (a) for Exp II and Exp III

(a)

Device	No.	Dimension		Comment
Tagging small counter	22	$0.5 \times 4 \times 1.7$ to $19.4\ cm^3$.		
Tagging large counter	14	$1 \times 4 \times 12$ to $45\ cm^3$.		
Recoil counter	23	$0.5 \times 3.3 \times 57.5\ cm^3$.	thick	
Front counter	4	$0.5 \times 15 \times 15\ cm^3$.	$\times$ wide	2.5 cm ϕ hole about beam axis
Back A-counter	4	$1 \times 30 \times 100\ cm^3$.	$\times$ long	
Back B-counter	5	$1 \times 30 \times 100\ cm^3$.		
Čerenkov counter	1	entrance window $1.0 \times 2.1\ m^2$ (height $\times$ width), viewed by six photomultipliers.		threshold was 1.6 GeV/c for pions.
Multiwire prop. chamber	2	$30 \times 30\ cm^2$, $60 \times 60\ cm^2$ (wide $\times$ long)		wire space = 2 mm
Spark chamber	8	$1 \times 1\ m^2$, the first two chambers were rotated by 45°.		wire space = 2 mm
Target center and front surface of beam stopper		2168 mm, 786 mm from the center of magnet, respectively.		

(b)

Device	No.	Dimension		Comment
Front counter	16	$0.5 \times 2 \times 30\ cm^3$	thick $\times$ wide $\times$ long	$2 \times 2\ cm^2$ hole about beam axis
Middle counter	12	$0.5 \times 12 \times 75\ cm^3$		
Multiwire prop. chamber	1	$60 \times 60\ cm^2$		wire space = 2 mm
Target center and front surface of beam stopper		1420 mm, 185 mm from the center of magnet, respectively.		

Table 2
A summary of the energy ranges used in these experiments

Period	Electron energy (GeV)	Photon energy (GeV)
Experiment I	7.2	4.65 – 6.70
Experiment II	5.5	3.0 – 5.0
Experiemnt III	5.2	3.0 – 4.5

portional chambers with vertical and horizontal readout were used; an additional array of 12 trigger counters was placed between the analysing magnet and the first spark chamber (M-hodoscope); the target and the beam stopper were moved deeper inside the spectrometer magnet and the recoil proton hodoscope was removed.

Details are also tabulated in table 1b.

3.2. *Tagging system*

The photon beam was generated by the bremsstrahlung of the electrons traversing the radiator. Their recoil electrons were deflected and passed through an array of three layers of scintillation counters which tagged the bremsstrahlung photons impinging on the hydrogen target. The first layer consisted of a picket-fence array of 22 scintillation counters each overlapping $\frac{1}{3}$ of its neighbour. This counter array separated the recoil momentum into 43 bins each with a width of 48.1 MeV. Thus

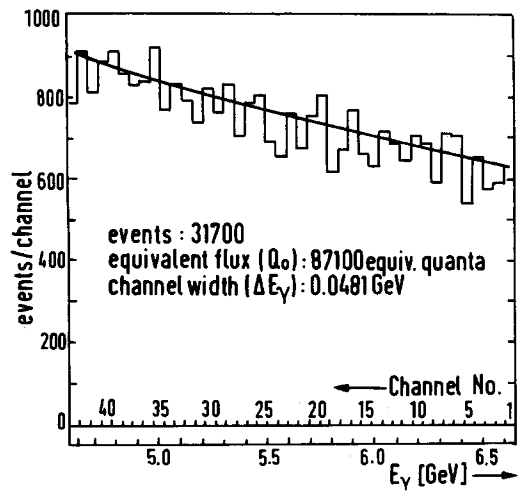

Fig. 3. The distribution of photons observed in the tagging channel. The solid curve represents an expected spectrum from the bremsstrahlung process.

the tagging system covered an energy band of photons over 2.02 GeV with a top energy of $E_{top} = E - 0.5$ GeV, where E is the energy of the incident electron beam.

The second and third layers consisted of 14 scintillation counters in pairs behind the first layer. They were used in two-fold coincidence in the trigger to give precise timing information and to monitor the flux of incident photons.

Calibration runs were made to investigate basic properties of the system: the energy calibration, the intensity dependence of the rate of multiple tags and the tagging efficiency. For the energy calibration, electron pairs produced in a thin target in front of the magnet by tagged photons were observed. By reconstructing the electron pair tracks, the energy of the pair was calculated and compared with the photon energy from the tagging system. Although the resolution of the pair spectrometer does not match the resolution of the tagging counters (±25 MeV), the center energy of each counter could be determined rather precisely to about ±10 MeV. This was also checked against the position of the recoil mass of an elastically produced ϕ meson.

The tagging efficiency, defined as the ratio of the number of photons arriving at the target position to that of electrons triggering the tagging system, was measured by placing a shower counter at the target position. The efficiency was (89 ± 2)%. At typical running conditions a beam of 2×10^5 tagged quanta per second (10% duty cycle) was used. The rate of multiple tags was 12% without accidental ones. Only single tags were accepted in the experiment. The measured cross section is based on the number of recorded single tags corrected for tagging efficiency. Fig. 3 shows an observed bremsstrahlung spectrum in the tagging window.

3.3. The Čerenkov counter

The counter consisted of a cylindrical steel tank with 2.40 m diameter and 2.33 m width positioned in the beam line behind the trigger counters with horizontal axis. Particles traversing the 2.1×1.0 m^2 steel entrance window of 3 mm thickness travelled through a radiator of about 1.7 m length. The light was focussed by 6 spherical mirrors of 70×70 cm^2 each with an aluminium light collector into the photocathodes of six 58-UVP phototubes through quartz windows. With freon-13 at 4 bar, the maximum Čerenkov angle (particles of the light speed) was 70 mrad. For these particles an angular divergence of ± 50 mrad could be accepted, which agrees with the divergence of the particle stream hitting the counter for momenta higher than 1.6 GeV (threshold for pions). The counter is shown in fig. 4.

The phototubes were run at 2.5 kV yielding pulses of about 1 volt for high energy electrons. The efficiency of the counter was measured by triggering the apparatus on two charged particles in front of and behind the magnet. By using the copiously produced ρ^0s, π mesons with momenta between 2 and 4 GeV were identified and the π meson signals in the Čerenkov counter were recorded. The test gave an average detection efficiency of (98 ± 2)%. Since the counter was used in veto mode, no effort was made to gain a more accurate number.

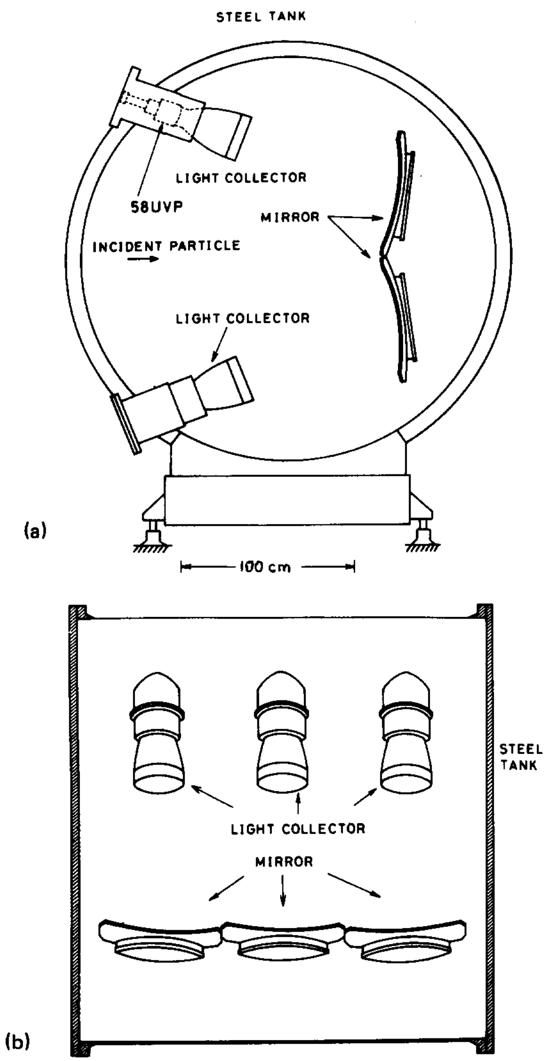

Fig. 4. Schematic drawings of the Čerenkov counter, (a) side view and (b) top view. The Čerenkov light is reflected and focussed by six mirrors into phototubes.

3.4. Data taking

An event was recorded when the following trigger requirement TR was fulfilled:

$$\mathrm{TR} = \mathrm{T}(\geqslant 1) \cdot \mathrm{F}(\geqslant 2) \cdot \mathrm{B}(\geqslant 2) \cdot \overline{\mathrm{C}} \qquad \text{in Exp I}\,,$$

$$\mathrm{TR} = \mathrm{T}(\geqslant 1) \cdot \mathrm{F}(\geqslant 2) \cdot M(\geqslant 2) \cdot \mathrm{B}(\geqslant 2) \cdot \overline{\mathrm{C}} \qquad \text{in Exp II and III}\,,$$

where

$T(\geqslant 1)$ is an OR-signal formed from a two-fold coincidence between any two overlapping back-up counters of the tagging system;

$F(\geqslant 2)$ is the majority coincidence that at least two of the front trigger counters have fired;

$M(\geqslant 2)$ is the majority coincidence that at least two counters of the M-hodoscope have fired;

$B(\geqslant 2)$ is the majority coincidence that at least two two-fold coincidences of overlapping counters occured in the trigger counters behind the spark chambers;

$\bar{C}$ is the absence of a signal from any of the six photomultipliers of the Čerenkov counter.

The spark chamber and proportional chamber addresses determining the particle traces, latches representing the status of all scintillation counters and the ADC's monitoring the pulse heights of the recoil hodoscope and of the Čerenkov counter photomultipliers were read *via* a CAMAC system into an on-line PDP-8/E computer, which furnished event and histogram displays and buffered the data before transferring it to magnetic tape *via* the DESY IBM 370/168 computer. The trigger rate was about ten triggers per 10^6 tagged quanta. The intensity of 2–4×10^5 tagged quanta per second was limited by the rates of the tagging system and the single rates in the front proportional chambers, which were irradiated by a large flux of pairs and Compton electrons The multiwire proportional chambers showed an accidental hit in every third or 4th strobe, which could be used for monitoring the beam position.

3.5. Data reconstruction

We identified, in a first step, particle trajectories using a pattern recognition program [8] taking events from our raw data sample carrying unique tagging information. With the help of a track fitting procedure two-prong events have been reconstructed simultaneously in both projections, using the corresponding signals identified in the multiwire-proportional- and spark chambers. The fit rendered particle momenta and the vertex coordinates. Fig. 5 shows orthogonal projections of reconstructed interaction points together with the physical boundaries of the target.

The Čerenkov information identified outgoing particles above threshold with a high probability as K mesons. Since the energy of the incoming gamma is also known, one can compute the missing mass and plot the invariant mass of the measured $K^{\pm}$ pair *versus* the mass of the recoil system. A two-dimensional plot for invariant K^+K^- mass *versus* recoil mass is shown in fig. 6, where the elastic ϕ signal shows up clearly.

Due to the association of the ϕ with higher recoil masses there is clear evidence for inelastic ϕ production. This evidence was confirmed through the recoil hodoscope, by which it could be proved, that the 'inelastic events' were not elastic with a falsly assigned gamma-energy. The kinematic separation of elastic from inelastic events could be obtained by selecting events which fell in both mass bands, the

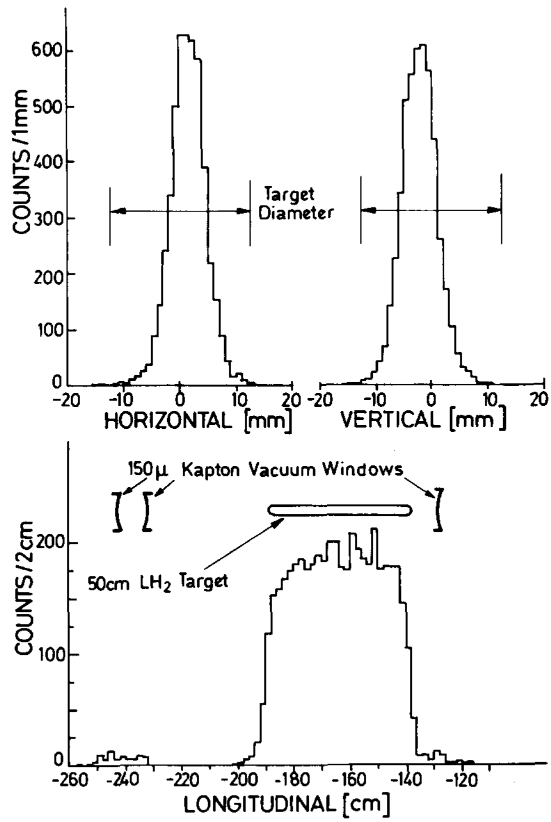

Fig. 5. The horizontal, vertical and longitudinal projections of the reconstructed vertices are compared with the target boundaries and the vacuum windows.

invariant K^+K^- mass around the ϕ meson ($1.01 \leqslant M_{KK} \leqslant 1.03$ GeV) and the recoil mass around the proton ($0 \leqslant M_X \leqslant 1.15$ GeV). The invariant K^+K^- mass distribution for a recoil mass in the proton band is shown in fig. 7.

As an alternative method for the kinematic separation we fitted the two-prong events applying the energy momentum constraint (1C fit). A probability distribution for the 1C kinematic fit is shown in fig. 8. From this distribution we selected elastic events with a confidence level of 0.95. Both methods gave essentially the same results.

The experimental width of the recoil proton peak (110 MeV FWHM) and of the ϕ mass peak (7 MeV FWHM) is consistent with our experimental momentum and energy resolution: $\sigma(p_{K^\pm}) \simeq 0.01\, p_{K^\pm}$ for $p = 3$ GeV and $\sigma(E_\gamma) = 25$ MeV. As a test for both the mass resolution and the calibration of the mass scale we analyzed a $K^0 \to 2\pi$ signal in our raw data sample. The invariant mass of two-prongs was evalu-

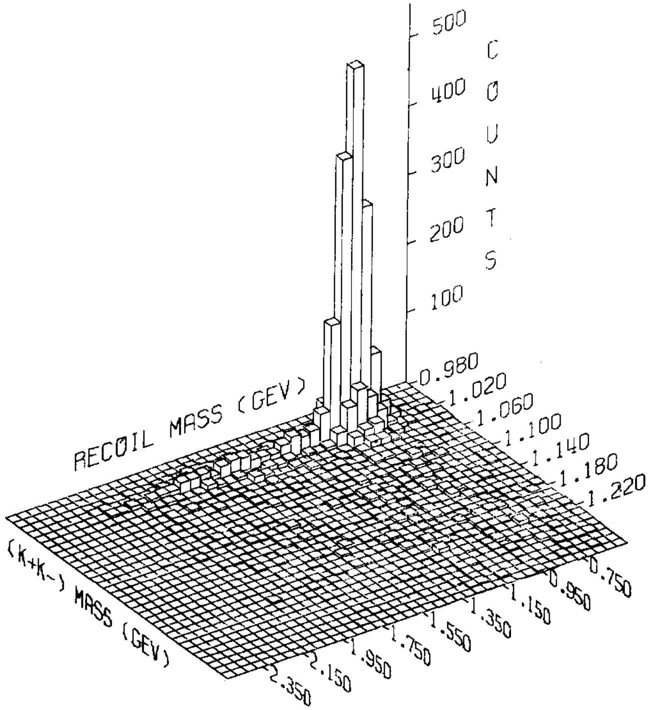

Fig. 6. The event distribution for invariant K^+K^- mass *versus* recoil mass.

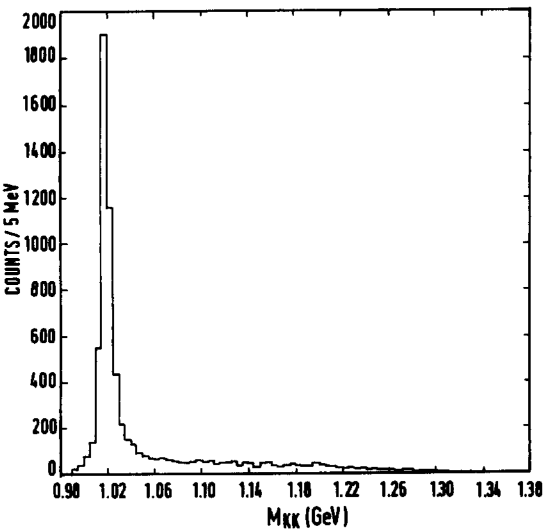

Fig. 7. The invariant K^+K^- mass distribution for recoil masses in the proton region

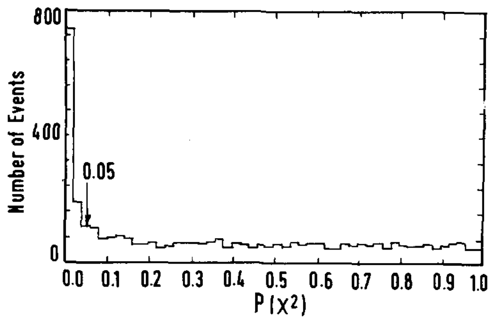

Fig. 8. Probability distribution for a 1C kinematic fit.

ated, where the momenta of both particles were below the Čerenkov threshold for pions and the interaction points were downstream of the end window of the target. The result is shown in fig. 9, where one recognizes the signal $K^0_S \to \pi^+\pi^-$ with a mass resolution of 6 MeV.

For the evaluation of the differential cross section $d\sigma/dt(\gamma p \to \phi p)$, the elastic data sample has been subjected to the following conditions: (i) all cuts with respect to charge, geometric boundaries and trigger conditions were applied again in the off-line analysis to the elastic data sample; (ii) the momenta of both particles had to be above Čerenkov threshold; (iii) to each event we assigned a detection efficiency which was computed with Monte Carlo technics, corresponding to the photon energy E_γ and the four-momentum transfer t (see subsect. 4.1). Events with detection efficiencies below 0.03 were rejected.

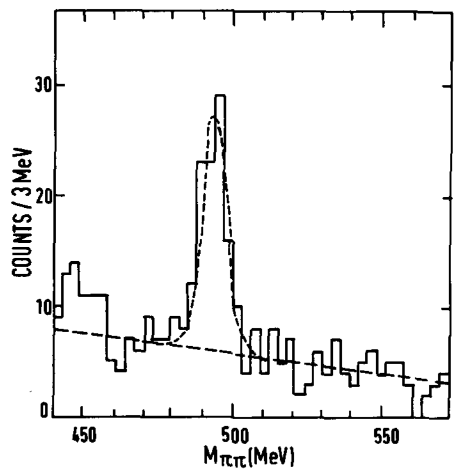

Fig. 9. The invariant $\pi^+\pi^-$ mass of events when both particle momenta were below the Čerenkov threshold and the vertex downstream of the target.

4. Differential cross section of the elastic ϕ production

4.1. Corrections

The differential cross section has been evaluated for bins Δt_i

$$\frac{d\sigma}{dt_i} = \frac{R_i}{F_i \Delta t_i} \frac{\epsilon}{n}, \tag{4.1}$$

with $R_i = N_i W_i$, where N_i is the number of events in the ith energy- and t-bin after background has been subtracted, W_i is a weight associated with each event calculated by Monte Carlo technics, F_i is the number of incident photons in the ith energy bin corrected for the bremsstrahlung distribution based on the counting rate in the seven big tagging channels, Δt_i is the bin size of the four-momentum transfer squared. The quantities n and ϵ are independent of the individual events: $n = \rho L_0 l/A$ is the number of protons per cm^2, where ρ is the liquid hydrogen density, L_0 is Loschmidt's number, l is the target length and A is the atomic weight of hydrogen (in gram). ϵ is a product of energy- and t-independent correction factors which are given below:

(i) losses due to knock-on electrons produced by a kaon in the window or radiator of the Čerenkov counter:	1.09 ± 0.02,
(ii) losses in the track recognition procedure:	1.04 ± 0.01,
(iii) losses due to the momentum and vertex reconstruction program:	1.12 ± 0.02,
(iv) losses due to multiprong events:	1.035 ± 0.01,
(v) losses due to single rate of the Čerenkov counter (veto rate):	1.02 ± 0.01,
(vi) losses due to hadronic interaction of hadrons in the target and scintillation counters:	1.02 ± 0.01,
(vii) losses due to counter inefficiencies:	1.01 ± 0.01,
(viii) correction for tagging efficiency and zeros and multiples in the small tagging counters:	1.28 ± 0.02,
(ix) correction for the branching ratio BR($\phi \to K^+K^-/\phi \to$ all):	2.14 .

The overall correction factor ϵ and its systematic error is thus 3.78 ± 0.14 which amounts to a 4% systematic error.

For the determination of $d\sigma/dt$ the t and E_γ dependent correction factors W_i have been computed using Monte Carlo technics. The following effects have been taken into account: the transverse distribution of the photon beam, the multiple scattering and nuclear absorption in all materials, energy loss in the target, the decay in flight of the kaon including corrections for the possibility that the secondaries from K decay cause a Čerenkov signal, the effective geometric and triggering acceptance and kaon momentum cuts.

It was assumed that the decay angular distribution of the ϕ meson has a $\sin^2\theta$ shape, where θ is the polar angle of K^+ in the helicity frame. This assumption was confirmed experimentally. For further discussion see sect. 5.

4.2. Analysis of the elastic cross section

About 4500 events in the energy range from 3.0 to 6.7 GeV have been selected falling in K^+K^- mass bins $1.01 \leqslant M_{KK} \leqslant 1.03$ GeV and in the recoil mass range $M_X \leqslant 1.15$ GeV. Using the methods and corrections described in subsect. 4.1 we obtained elastic differential cross sections which are presented in fig. 10 and table

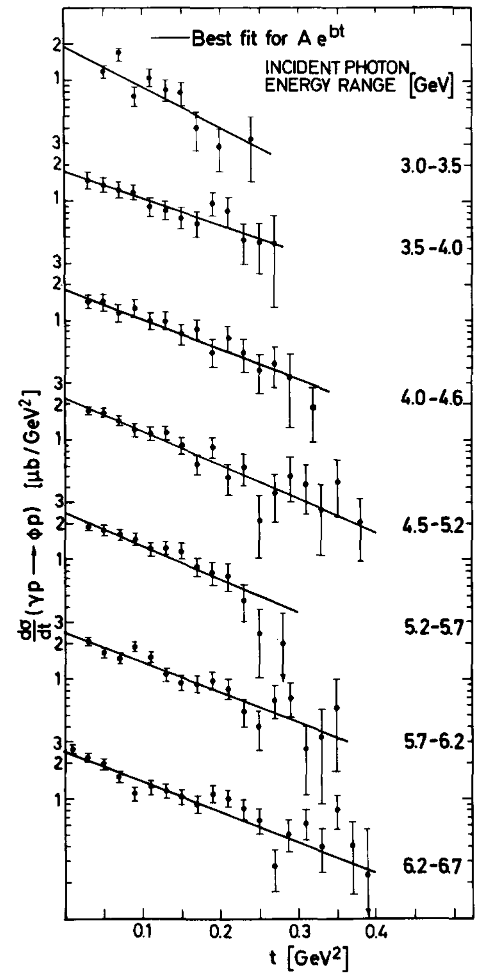

Fig. 10. The t-dependence of the differential cross section for the elastic process at different photon energies. The straight lines are fits to a linear exponential form.

Table 3
The elastic differential cross sections in $\mu b/GeV^2$

$\lvert t \rvert$ (GeV^2)	Incident photon energy (GeV)						
	3.0 – 3.5	3.5 – 4.0	4.0 – 4.5	4.5 – 5.1	5.1 – 5.6	5.6 – 6.2	6.2 – 6.7
0.01							2.63 ± 0.21
0.03		1.51 ± 0.23	1.44 ± 0.17	1.76 ± 0.12	1.86 ± 0.14	2.06 ± 0.16	2.20 ± 0.18
0.05	1.19 ± 0.13	1.36 ± 0.71	1.42 ± 0.21	1.69 ± 0.14	1.75 ± 0.16	1.65 ± 0.16	1.96 ± 0.19
0.07	1.65 ± 0.20	1.23 ± 0.19	1.18 ± 0.21	1.45 ± 0.14	1.60 ± 0.16	1.49 ± 0.15	1.51 ± 0.16
0.09	0.74 ± 0.14	1.19 ± 0.19	1.27 ± 0.20	1.21 ± 0.14	1.47 ± 0.16	1.87 ± 0.17	1.09 ± 0.14
0.11	1.06 ± 0.18	0.90 ± 0.16	0.98 ± 0.17	1.13 ± 0.14	1.21 ± 0.15	1.52 ± 0.16	1.23 ± 0.16
0.13	0.85 ± 0.18	0.85 ± 0.16	0.98 ± 0.17	1.14 ± 0.14	1.24 ± 0.16	1.09 ± 0.14	1.16 ± 0.16
0.15	0.79 ± 0.18	0.73 ± 0.16	0.77 ± 0.15	0.87 ± 0.14	1.17 ± 0.17	0.93 ± 0.14	1.03 ± 0.15
0.17	0.41 ± 0.15	0.65 ± 0.16	0.84 ± 0.16	0.62 ± 0.13	0.87 ± 0.15	0.91 ± 0.15	0.90 ± 0.15
0.19	0.90 ± 0.28	0.97 ± 0.22	0.55 ± 0.14	0.85 ± 0.15	0.78 ± 0.17	0.97 ± 0.16	1.07 ± 0.17
0.21	0.17 ± 0.12	0.82 ± 0.23	0.72 ± 0.17	0.48 ± 0.14	0.73 ± 0.19	0.83 ± 0.16	1.00 ± 0.17
0.23	0.85 ± 0.40	0.48 ± 0.17	0.52 ± 0.16	0.59 ± 0.17	0.45 ± 0.16	0.53 ± 0.14	0.81 ± 0.16
0.25	0.20 ± 0.20	0.45 ± 0.20	0.38 ± 0.14	0.21 ± 0.11	0.24 ± 0.14	0.40 ± 0.14	0.65 ± 0.16
0.27		0.44 ± 0.32	0.44 ± 0.16	0.36 ± 0.16	0.17 ± 0.18	0.66 ± 0.20	0.27 ± 0.10
0.29			0.33 ± 0.20	0.49 ± 0.21	0.26 ± 0.26	0.69 ± 0.23	0.49 ± 0.16
0.31			0.19 ± 0.12	0.42 ± 0.19		0.26 ± 0.15	0.62 ± 0.18
0.33			0.18 ± 0.13	0.26 ± 0.15		0.33 ± 0.24	0.40 ± 0.17
0.35				0.45 ± 0.23		0.57 ± 0.41	0.80 ± 0.26
0.37				0.48 ± 0.24			0.41 ± 0.24
0.39				0.13 ± 0.13			0.23 ± 0.23
$\left.\frac{d\sigma}{dt}\right\rvert_0 \left(\frac{\mu b}{GeV^2}\right)$	1.96 ± 0.26	1.74 ± 0.19	1.86 ± 0.17	2.23 ± 0.13	2.42 ± 0.16	2.44 ± 0.15	2.52 ± 0.13
Slope (GeV^{-2})	7.76 ± 1.27	5.13 ± 0.96	5.79 ± 0.68	6.45 ± 0.54	6.36 ± 0.63	5.76 ± 0.52	5.88 ± 0.44

The optical points and the slope values are fitted values assuming a linear exponential t-dependence.

3. The straight lines in fig. 10 are best fits to the data using an exponential form

$$\frac{\mathrm{d}\sigma}{\mathrm{d}t} = \left(\frac{\mathrm{d}\sigma}{\mathrm{d}t}\right)_{t=0} \exp(-B|t|) \,. \tag{4.2}$$

The best fit values for the extrapolated forward cross sections to $t = 0$ $(\mathrm{d}\sigma/\mathrm{d}t)_0$ and the slope value B are listed also in table 3. Whereas the cross section measurements of this experiment agree with other measurements in overlapping t regions ($|t| \simeq 0.4$ GeV^2), a significant steepening of the differential cross section was observed at forward direction.

The slopes of our experimental t-distributions are found to be significantly larger than those reported by previous ϕ photoproduction experiments [2] which in most cases did not cover the small t-region. This fact is substantiated by the single energy measurement of the Cornell group * in the same t-region as this experiment.

The extrapolated cross section intercepts (optical points) $(\mathrm{d}\sigma/\mathrm{d}t)_0$ at our energy range show an energy dependence. In fig. 11 $(\mathrm{d}\sigma/\mathrm{d}t)_0$ is plotted as a function of E_γ together with values obtained in other experiments [2]. A simple explanation for this energy dependence can be found in applying the VDM relation (2.4). If one assumes that

$$C = \frac{\alpha}{64\pi} \frac{4\pi}{\gamma_\phi^2} (1 + \eta_\phi^2)\, \sigma_{\mathrm{tot}}^2(\phi \mathrm{p}) \tag{4.3}$$

is constant in our energy range, we can fit the optical points of this experiment (including the threshold point) to the relation

$$\left(\frac{\mathrm{d}\sigma}{\mathrm{d}t}\right)_0 = C\left(\frac{p_\phi}{k}\right)^2_{\mathrm{CM}} \,. \tag{4.4}$$

We obtained the result (fig. 11) $C = 2.93 \pm 0.08\ \mu\mathrm{b/GeV}^2$. This result explains the energy dependence of our data and is in excellent agreement with all other published optical points in this energy range. In addition it supports the assumption that $(1 + \eta_\phi^2)\, \sigma_{\mathrm{tot}}^2(\phi \mathrm{p})$ is essentially energy independent in the energy range considered.

Furthermore, since the product of $(\gamma_\phi^2/4\pi)^{-1}$ and $\sigma_{\mathrm{tot}}(\phi \mathrm{p})$ is fixed by the above value of C (for η we used the value 0.06 determined in a recent experiment [9]), our experiment establishes a correlation between the γ_ϕ coupling constant and $\sigma_{\mathrm{tot}}(\phi \mathrm{p})$ which can be compared to values of $\sigma_{\mathrm{tot}}(\phi \mathrm{p})$ and $\gamma_\phi^2/4\pi$ obtained both with different methods and in other experiments. Fig. 12 shows the curve which corresponds to the C value obtained in this experiment. The plot shows also the $\mathrm{e}^+\mathrm{e}^-$ annihilation value for $\gamma_\phi^2/4\pi$ [10] and of $\sigma_{\mathrm{tot}}(\phi \mathrm{p})$ obtained by ϕ photoproduction on C^{12} (ref. 2(D-MIT)).

* The authors of (C-72) in ref. [2] gave the slope value 5.4 ± 0.3 GeV^{-2} assuming a linear exponential form of the t-distribution in $0.08 \leqslant t \leqslant 0.52$ GeV^2.

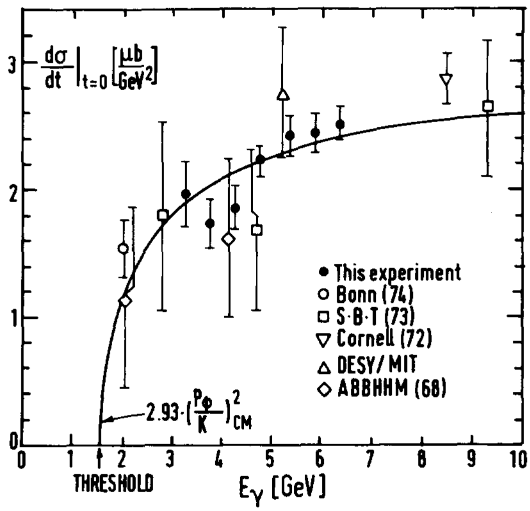

Fig. 11. The energy dependence of the optical point. The curve is the best fit to the data of this experiment.

In addition fig. 12 shows upper and lower bounds of $\sigma_{tot}(\phi p)$ by computing quark sum rules for $\sigma(\phi p)$ from total hadronic cross sections extrapolated from NAL energies into the 2–10 GeV region [11].

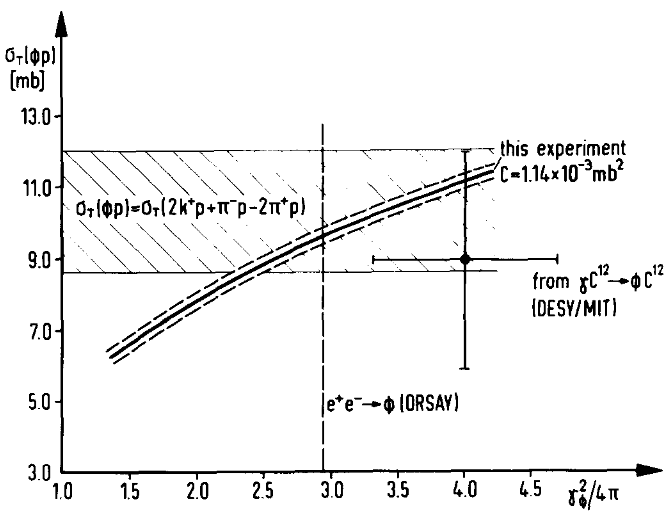

Fig. 12. Relation between σ_{tot} and $\gamma_\phi^2/4\pi$ due to eq. (4.3) represented by $C = (1.14 \pm 0.03) \times 10^{-3}$ mb^2 as determined in this experiment.

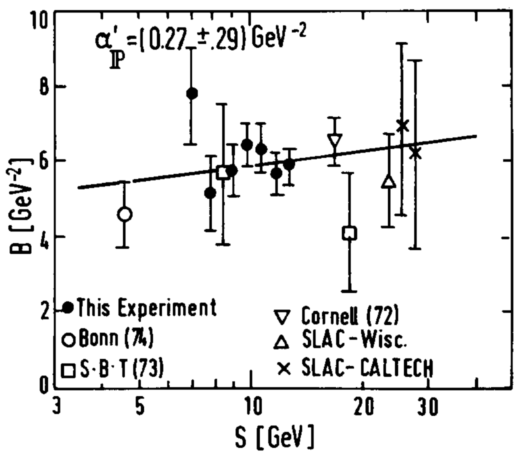

Fig. 13. A fit of B of the relation (4.5) as a function of s in the region $|t| \leqslant 0.4\ \mathrm{GeV}^2$.

4.3. *The slope of the pomeron*

The analysis of the ϕ cross section yields information on the properties of the pomeron trajectory as discussed in sect. 2. Because of the observed t-dependence of the slope B, the analysis of the pomeron slope was confined to the forward region of the differential cross section.

Using only data with $t \leqslant 0.4\ \mathrm{GeV}^2$, all available experimental results * have been refitted to the form $A\ \exp(-B|t|)$. Fig. 13 and table 4 present the results of these fits. The straight lines in fig. 13 are the best fit to the form

$$B = a + 2\alpha'(0)\ \ln(s/s_0)\ , \tag{4.5}$$

with $a = 4.2 \pm 1.4\ \mathrm{GeV}^{-2}$ and $\alpha'(0) = 0.27 \pm 0.29\ \mathrm{GeV}^{-2}$, which is essentially consistent with 'no shrinkage'. This result is consistent with that at $t = 0.6\ \mathrm{GeV}^2$ obtained by combined cross sections from SLAC and Bonn data **.

The significance of this result is limited since we only used data in a comparatively small s region. For hadron induced reactions at FNAL-energies the slope value [12] of the pomeron trajectory was obtained to $\alpha'(0) \simeq 0.2\ \mathrm{GeV}^{-2}$ at $t = 0.2\ \mathrm{GeV}^2$.

In order to improve the statistics and to increase the energy range, the world data on ϕ photoproduction were grouped into three energy bins as shown in table 5. In each bin the slope value of the differential cross section was evaluated at $|t| = 0.2\ \mathrm{GeV}^2$ by fitting the data over the whole t-region to the form $\mathrm{d}\sigma/\mathrm{d}t \propto \exp(a|t| + bt^2)$.

* Experimental values for $\mathrm{d}\sigma/\mathrm{d}t$ have been obtained through private communication for all but (S-W) in ref. [2]. The data of (S-W) have been taken from their graph.

** See (BONN) and (S-W) in ref. [2].

Table 4

Fitted slope values obtained for other ϕ photoproduction experiments with a linear exponential fit to the limited range $|t| \leqslant 0.4$ GeV^2

Experiment	Photon energy (GeV)	s (GeV^2)	Slope ($|t| < 0.4$) (GeV^{-2})
Bonn	2	4.64	4.55 ± 0.85
S.B.T.	2.8 + 4.7	8.4	5.67 ± 1.83
C-72	8.5	16.9	6.55 ± 0.58
S-W	9.3	18.4	4.16 ± 1.56
S-CT	12	23.4	5.49 ± 1.20
	13	25.3	6.83 ± 2.29
	14	27.1	6.22 ± 2.47

Table 5

Fitted slope values at $t = 0.2$ GeV^2 of several experiments referenced in [2]

Experiment	Photon energy (GeV)	s (GeV^2)	Slope at $|t| = 0.2$ GeV^2 (GeV^{-2})
D-K	3.0 – 5.6	9.0	5.81 ± 0.20
S-B-T	2.8 – 4.7		
D-BC	2.5 – 5.8		
D-MIT	5.2		
D-K	5.6 – 6.7	12.6	5.22 ± 0.19
S-CT	6.0 – 6.5		
S-B-T	9.3	17.6	5.86 ± 0.24
C-72	8.5		
S-W	9.0		

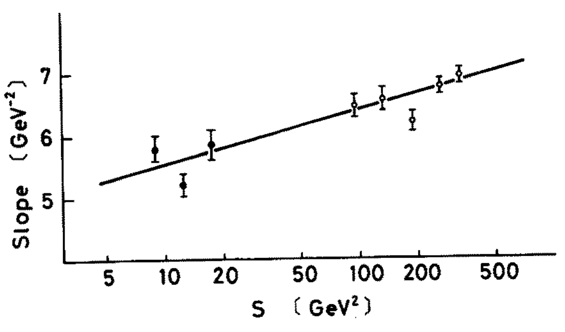

Fig. 14. The slope value B at $|t| = 0.2$ GeV^2 plotted as a function of s. The black points are obtained from photoproduction data and the open circles are from ref. [25]. The solid curve represents an effective slope from "$\phi p \to \phi p$": 0.19 ± 0.02 GeV^2.

The result is given in table 5.

It is interesting to compare the pomeron related slopes (4.5) obtained in ϕ photoproduction with the same quantity obtained in purely hadronic reactions at much higher energies. In ref. [25] the authors have computed B for 'ϕp' scattering from elastic hadronic cross sections measured at FNAL energies, using the SU(3) relation with ideal mixing. The slope value obtained from the photoproduction data appears to be consistent to that derived from the hadronic reactions, although one has to bear in mind that there is a systematic difference in evaluating B from ϕ photoproduction and from the experiments of ref. [25]. By fitting the points in fig. 14 to the form (4.5), one gets $a = 4.66 \pm 0.22\ \mathrm{GeV}^{-2}$ and $\alpha'(0) = 0.19 \pm 0.02\ \mathrm{GeV}^{-2}$. The solid curve in fig. 14 is based on the fitted values.

5. Spin density analysis in the ϕ region

The geometric acceptance of our experimental set up has a reasonable efficiency for the entire range of the polar decay angle θ of the kaon measured in the K^+K^- rest system. Hence for kinematic reconstructed events it was possible to study the spin structure of the K^+K^- system, in particular to evaluate spin density matrix elements of the ϕ as a function of the four-momentum transfer t and E_γ.

For the evaluation of the spin density matrix elements ρ_{ik} we applied two essentially equivalent methods:

(i) For the ϕ being a spin-1 resonance which decays into two spinless particles (kaons), the decay distribution can be expressed in terms of the spin density elements ρ_{ik} as follows [13]:

$$I(\theta, \phi) = \frac{3}{4\pi} \{\rho_{00} \cos^2\theta + \rho_{11} \sin^2\theta - \rho_{1-1} \sin^2\theta \cos 2\phi - \sqrt{2}\,\mathrm{Re}(\rho_{10}) \sin 2\theta \cos\phi)\} ,$$
$$\rho_{00} = 1 - 2\rho_{11} , \tag{5.1}$$

where θ and ϕ are the polar and azimuthal decay angles of the K^+ in the rest-system of the ϕ. I is normalized with the total number of events. The experimental data have been fitted to the relation (5.1) by optimizing the parameters ρ_{ik} using least square and likelihood methods.

(ii) The ρ_{ik} have also been evaluated by computing numerically moments of spheri cal harmonics $\langle Y_L^M \rangle$ from the acceptance corrected experimental decay distribution $I_c(\theta, \phi)$, normalized to the total number of events:

$$\frac{\langle Y_L^M \rangle}{\langle Y_0^0 \rangle} = \int I_c(\theta, \phi)\, Y_L^M(\theta, \phi)\, d\Omega . \tag{5.2}$$

The ρ_{ik} for $J = 1$ are then related to the moments in the following way:

$$\rho_{00} = \tfrac{1}{3}\left(\sqrt{5}\,\frac{\langle Y_2^0 \rangle}{\langle Y_0^0 \rangle} + 1\right),$$

$$\rho_{1-1} = -\sqrt{\tfrac{5}{6}}\,\mathrm{Re}\,\frac{\langle Y_2^2 \rangle}{\langle Y_0^0 \rangle}, \qquad (5.3)$$

$$\mathrm{Re}(\rho_{10}) = \sqrt{\tfrac{5}{12}}\,\mathrm{Re}\,\frac{\langle Y_2^1 \rangle}{\langle Y_0^0 \rangle}.$$

The decay angular distributions have been studied with respect to two reference frames. In the *s-channel or helicity* (H) system the axis of quantisation corresponds to the direction of the outgoing phi as seen in the overall center of momentum system. In the *t-channel or Gottfried-Jackson* (GJ) system [14] the axis of quantisation corresponds to the direction of the incident photon as seen in the phi-meson rest system (see fig. 15).

By convention the angle between the direction of the K^+ meson and the z-axis is the helicity polar angle θ and the angle between the x axis and the projection of the K^+ direction on the xy plane is the helicity azimuthal angle. Experimental efficiencies, related to geometric and decay in flight losses, have been computed with Monte Carlo technics for a multidimensional grid of the kinematic variables ($M_{K^+K^-}$, E_γ, t, θ, ϕ). Inverse efficiencies were used as weight factors for the experimental events grouped in corresponding bins.

Using the methods described before we evaluated density matrix elements ρ_{ik}^{H} and ρ_{ik}^{GJ} referring to both coordinate systems, the H and GJ frames, respectively. The kin

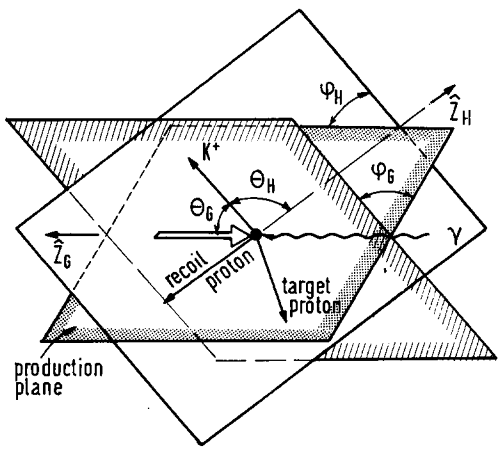

Fig. 15. Definition of decay angles in the helicity and Gottfried-Jackson system.

Table 6
The spin density matrix elements for the elastic data, (a) in the helicity frame and (b) in the Gottfried-Jackson frame

(a) Helicity system

Photon energy (GeV)		4.65 – 5.68			5.68 – 6.71	
$\lvert t - t_{min} \rvert$ (GeV^2)	ρ_{00}	Re ρ_{10}	ρ_{1-1}	ρ_{00}	Re ρ_{10}	ρ_{1-1}
0.00 – 0.04	−0.05 ± 0.03	−0.04 ± 0.03	−0.03 ± 0.04	−0.02 ± 0.03	−0.01 ± 0.03	−0.07 ± 0.04
0.04 – 0.08	0.00 ± 0.03	−0.05 ± 0.03	−0.10 ± 0.05	0.00 ± 0.03	−0.03 ± 0.03	−0.08 ± 0.05
0.08 – 0.12	0.03 ± 0.06	−0.05 ± 0.04	0.10 ± 0.07	0.02 ± 0.04	−0.07 ± 0.03	0.00 ± 0.06
0.12 – 0.16	0.00 ± 0.06	0.00 ± 0.04	0.04 ± 0.08	−0.01 ± 0.05	−0.08 ± 0.05	−0.03 ± 0.07
0.16 – 0.20	0.07 ± 0.10	−0.03 ± 0.07	−0.02 ± 0.11	−0.02 ± 0.03	−0.07 ± 0.03	0.10 ± 0.09
0.20 – 0.24				0.04 ± 0.08	0.01 ± 0.06	−0.11 ± 0.09

(b) Gottfried-Jackson system

Photon Energy (GeV)		4.65 – 5.68			5.68 – 6.71	
$\lvert t - t_{min} \rvert$ (GeV^2)	ρ_{00}	Re ρ_{10}	ρ_{1-1}	ρ_{00}	Re ρ_{10}	ρ_{1-1}
0.00 – 0.04	−0.03 ± 0.04	0.08 ± 0.03	−0.02 ± 0.04	0.02 ± 0.04	0.11 ± 0.03	−0.05 ± 0.04
0.04 – 0.08	0.09 ± 0.05	0.16 ± 0.03	−0.05 ± 0.05	0.11 ± 0.05	0.16 ± 0.03	−0.03 ± 0.05
0.08 – 0.12	0.11 ± 0.05	0.11 ± 0.04	0.14 ± 0.06	0.11 ± 0.05	0.15 ± 0.04	0.04 ± 0.06
0.12 – 0.16	0.24 ± 0.08	0.16 ± 0.05	0.16 ± 0.07	0.15 ± 0.08	0.19 ± 0.05	0.05 ± 0.07
0.16 – 0.20	0.29 ± 0.07	0.15 ± 0.04	0.09 ± 0.07	0.14 ± 0.07	0.16 ± 0.04	0.18 ± 0.07
0.20 – 0.24				0.42 ± 0.10	0.18 ± 0.07	0.08 ± 0.08

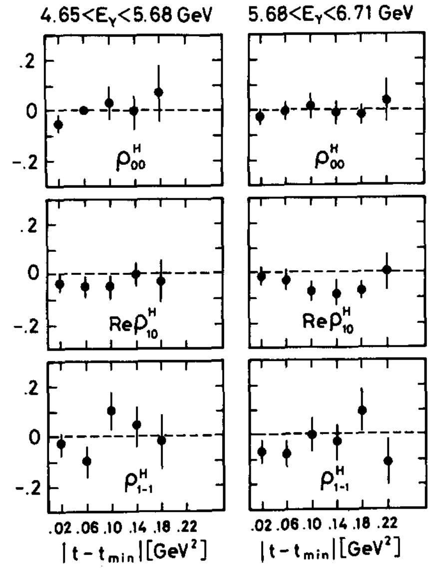

(a)

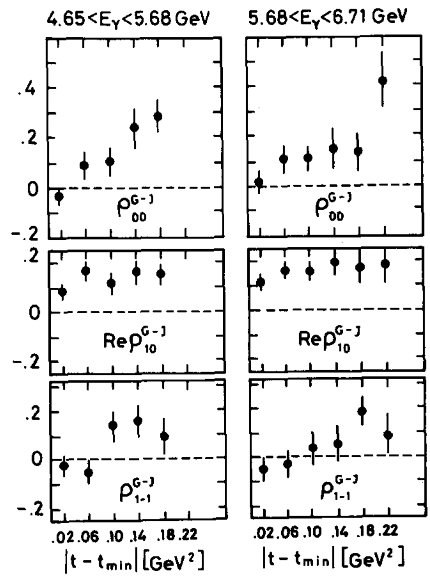

(b)

Fig. 16. t-dependence of the ϕ spin density matrix elements evaluated for two energy regions; (a) in the helicity frame, (b) in the Gottfried-Jackson frame.

matic regions of this analysis were

$$1.01 \leqslant M_{K^+K^-} \leqslant 1.03 \text{ GeV} ,$$

$$4.66 \leqslant E_\gamma \leqslant 6.70 \text{ GeV} , \qquad (2 \text{ bins}) ,$$

$$0 \leqslant |t - t_{min}| \leqslant 0.2 \text{ GeV}^2 , \qquad (4 \text{ bins}) .$$

The results which we obtained from the different fitting procedures were consistant within the errors. The results are listed in tables (6a) and (6b) and plotted in figs. 16a and 16b.

For conservation of the s-channel helicity (SHC) one expects for photoproduced ϕ mesons a $\sin^2\theta^H$ distribution of the decay in the H-frame which is independent of t The experimental decay distribution of the ϕ showing a $\sin^2\theta$ shape confirms SHC

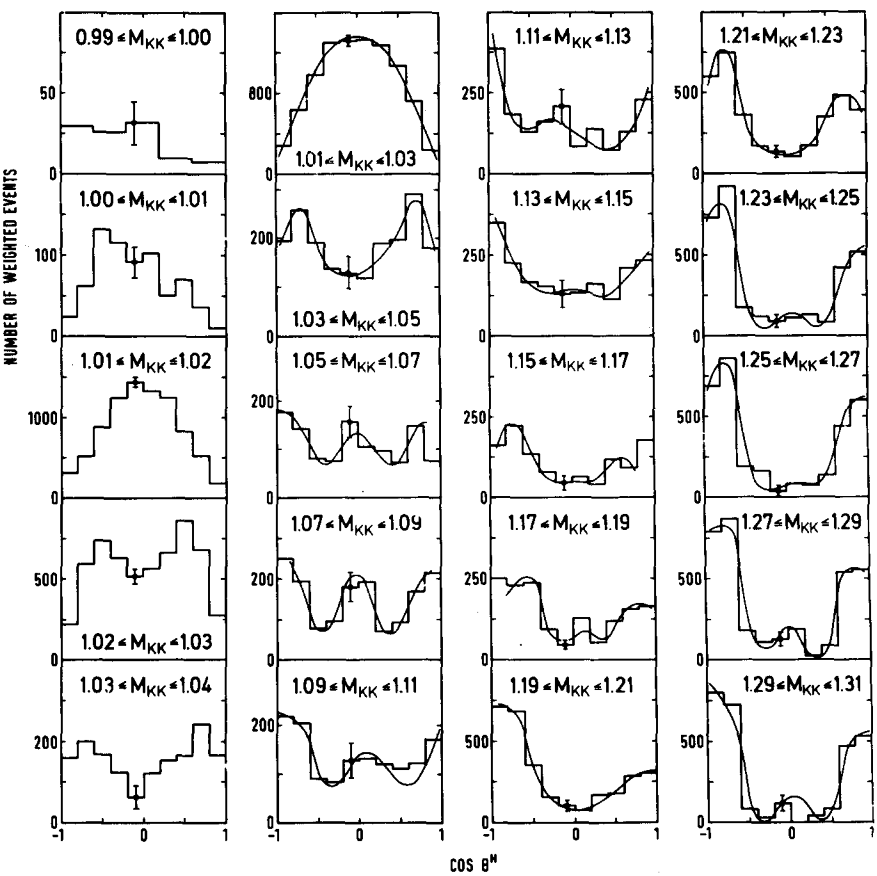

Fig. 17. K^+K^- decay angular distributions in the helicity frame as a function of the invariant K^+K^- mass. Solid lines are fits of a superposition of Legendre polynomials to the data.

(see fig. 17, $1.01 \leqslant M_{KK} \leqslant 1.03$ GeV). ρ^{H}_{00} is essentially zero in the t range considered whereas the corresponding element in the GJ frame shows a clear t dependence.

The fact that the off-diagonal elements ρ^{H}_{1-1}, Re ρ^{H}_{10} which are related to spin-flip contributions in the ϕ production show slight deviations from zero, indicates the presence of other than SHC amplitudes contributing to the K^+K^- spectrum. In particular the significant deviation of ρ^{GJ}_{10} from zero represents the presence of unnatural parity exchange (see sects. 6, 7).

6. Helicity amplitudes for diffractive ϕ photoproduction

The density matrix elements and the differential cross section evaluated in this experiment have been used to carry out an analysis of the helicity amplitudes which contribute to the ϕ photoproduction. This analysis is based on a Regge model for the photoproduction and decay of vector mesons which was developed by P. Schlamp [15] and has been used by I. Derado et al. [16] for an analysis of ρ^0 photoproduction. The model is restricted to the exchange of even signature, natural parity trajectories. (For details of the model see ref. [18]). The t-channel helicity amplitudes are then defined by

$$f^{t}_{\lambda_\phi\lambda_\gamma\lambda_{\bar{p}}\lambda_p} = \gamma_{\lambda_\phi\lambda_\gamma\lambda_{\bar{p}}\lambda_p}(t)\, b_{\lambda\mu}(t)\, \frac{1+e^{-i\pi\alpha(t)}}{\sin \pi\alpha(t)} \left(\frac{s}{s_0}\right)^{\alpha(t)-\lambda_{\max}} , \tag{6.1}$$

with scaling constant $s_0 = 1\ \mathrm{GeV}^2$, $\lambda = \lambda_{\bar{p}} - \lambda_p$, $\mu = \lambda_\phi - \lambda_\gamma$ and $\lambda_{\max} = \max(|\lambda|, |\mu|)$. The terms $b_{\lambda\mu}(t)$ take into account kinematic and Regge singularities and contain also dimension factors to make the amplitudes dimensionless. $\gamma_{\lambda_\phi\lambda_\gamma\lambda_{\bar{p}}\lambda_p}(t)$, which is proportional to the residue function, has been parametrized as follows:

$$\gamma_{\lambda_\phi\lambda_\gamma\lambda_{\bar{p}}\lambda_p}(t) = g \exp(-a|t| - bt^2)\, r_{\lambda_\phi\lambda_\gamma\lambda_{\bar{p}}\lambda_p} , \tag{6.2}$$

where constants g, a and b depend on the exchange trajectory $\alpha(t)$. The $r_{\lambda_\phi\lambda_\gamma\lambda_{\bar{p}}\lambda_p}$ are constants depending only on the helicity states of incoming and outgoing particles.

In our analysis only the pomeron exchange was considered. Hence $\alpha(t)$ was parametrized as

$$\alpha(t) = 1 + \alpha'(0)\, t .$$

As far as the helicity dependent constants are concerned, only three of them are free parameters, $r_{1\ 1\ 1/2\ -1/2}$, $r_{0\ 1\ 1/2\ -1/2}$ and $r_{-1\ 1\ 1/2\ 1/2}$ (because of the overall normalization g one can set $r_{1\ 1\ 1/2\ 1/2} = 1$). Thus we get six independent helicity amplitudes in the t-channel using the free parameters above. The explicit form of the amplitudes (6.2) can be found in ref. [18].

The physical quantities, i.e. the differential cross sections and the density matrix elements are related to these amplitudes in the following way:

$$\frac{d\sigma}{dt} = \frac{1}{8\pi(s-M^2)^2} \sum_{\lambda_\phi\lambda_\gamma\lambda_{\bar{p}}\lambda_p} f^t_{\lambda_\phi\lambda_\gamma\lambda_{\bar{p}}\lambda_p} f^{t*}_{\lambda_\phi\lambda_\gamma\lambda_{\bar{p}}\lambda_p} , \tag{6.3}$$

$$\rho^H_{\lambda_\phi\lambda'_\phi} = \frac{1}{N} \sum_{\lambda'_p\lambda_\gamma\lambda_p} f^s_{\lambda_\phi\lambda_p'\lambda_\gamma\lambda_p} f^{s*}_{\lambda'_\phi\lambda_p'\lambda_\gamma\lambda_p} , \tag{6.4}$$

$$\rho^{GJ}_{\lambda_\phi\lambda'_\phi} = \frac{1}{N} \sum_{\lambda_{\bar{p}}\lambda_p\lambda_\gamma} f^t_{\lambda_\phi\lambda_\gamma\lambda_{\bar{p}}\lambda_p} f^{t*}_{\lambda'_\phi\lambda_\gamma\lambda_{\bar{p}}\lambda_p} , \tag{6.5}$$

$$N = \sum_{\lambda_\phi\lambda_p'\lambda_\gamma\lambda_p} f^s_{\lambda_\phi\lambda_p'\lambda_\gamma\lambda_p} f^{s*}_{\lambda_\phi\lambda_p'\lambda_\gamma\lambda_p} , \tag{6.6}$$

where sufficies H and GJ denote helicity frame and Gottfried-Jackson system, respectively. The helicity amplitudes for the s-channel $f^s_{\lambda_\phi\lambda_p'\lambda_\gamma\lambda_p}$ are obtained by means of the crossing relation [17] from $f^t_{\lambda_\phi\lambda_\gamma\lambda_{\bar{p}}\lambda_p}$ (See eq. (17) in ref. [18]).

By fitting eq. (6.4) to the experimental density matrix elements in the helicity frame, three sets of the helicity-dependent constants $r_{\lambda_\phi\lambda_\gamma\lambda_{\bar{p}}\lambda_p}$ have been evaluated by making assumptions about α'. The three cases considered are:

(A) $\alpha'(0) = 0.22\ \mathrm{GeV}^{-2}$ from the pp result [18],

(B) $\alpha'(0) = 0.27\ \mathrm{GeV}^{-2}$ from the result in equation (4.4),

(C) $\alpha'(0)$ = free parameter .

The results are listed in table 7a for each case [19].

Table 7
Fit parameters of the helicity amplitudes for different assumptions described in sect. 6

Fit condition	$\alpha'(0)$	$r_{11\ 1/2\ -1/2}$	$r_{01\ 1/2\ 1/2}$	$r_{11\ 1/2\ 1/2}$	χ^2/DF
A	0.22	0.10 ± 0.66	2.26 ± 0.15	−30.90 ± 10.41	12.2/14
B	0.27	0.01 ± 0.17	2.23 ± 0.15	−25.36 ± 8.39	12.2/14
C	0.23 ± 0.50	0.05 ± 0.54	2.25 ± 0.17	−30.83 ± 75.68	12.2/13
Fit condition	g	a	b	χ^2/DF	t-dependence
D	8.58 ± 0.09	1.43 ± 0.09	0.58 ± 0.11	171.8/78	$e^{-(a\|t\|+bt^2)}$
E	8.91 ± 0.07	1.90 ± 0.03	0	203.8/79	$e^{-a\|t\|}$

Using the parameter set obtained for the case (A), the parameters g, a and b were obtained by fitting eq. (6.3) to a compilation of all published ϕ data [2]. Here again we distinguish 2 cases:

(D) g, a and b are free parameters,

(E) g and a are free parameters and $b = 0$.

The fitting results are listed in table 7b.

The ρ_{ik}^{H} calculated theoretically on the basis of (6.4) for the case (A) are plotted in fig. 18 as solid curves passing through the experimental values of ρ_{ik}^{H}. The corresponding density matrix elements in the Gottfried-Jackson system from eq. (6.4) are also given by the solid curves in fig. 18, together with the experimental points.

The theoretical cross sections due to eq. (6.3) fitted for the assumptions (D) and (E) are drawn in fig. 19. In this figure, an experimental curve fitted with data only for $|t| > 0.4\ \mathrm{GeV}^2$ is presented for a comparison with experimental results for $|t| \leqslant 0.4\ \mathrm{GeV}^2$.

The helicity amplitudes evaluated for the assumptions (A) and (D) for both s-

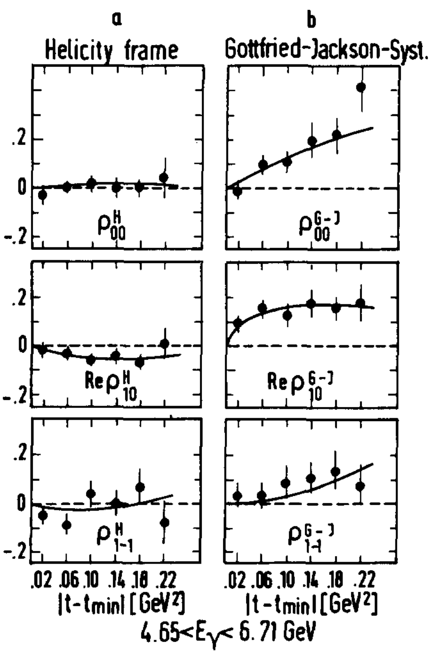

Fig. 18. Spin density matrix elements computed from the diffractive helicity amplitudes (sect. 6) together with experimental results; (a) in the helicity frame and (b) in the Gottfried-Jackson system.

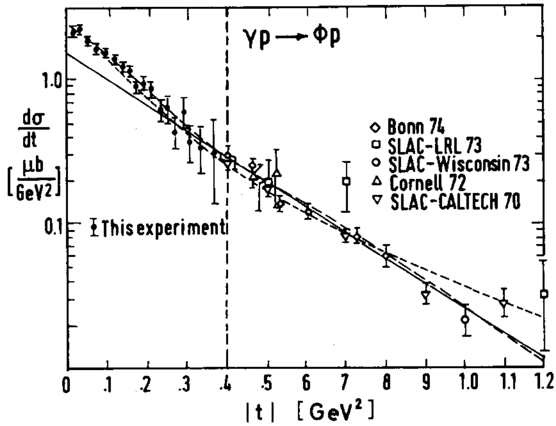

Fig. 19. The elastic differential cross sections are plotted as a function of t together with other experimental results. The curves obtained on the basis of the helicity amplitude analysis (sect. 6) are drawn for the assumptions D (dashed line ---) and E (longer dash —). A linear exponential fit to the data in the region $t > 0.4$ GeV^2, yielding an intercept of 1.44 ± 0.16 GeV^2 and a slope of $B = 4.05 \pm 0.19$ GeV^{-2} are drawn as a solid line.

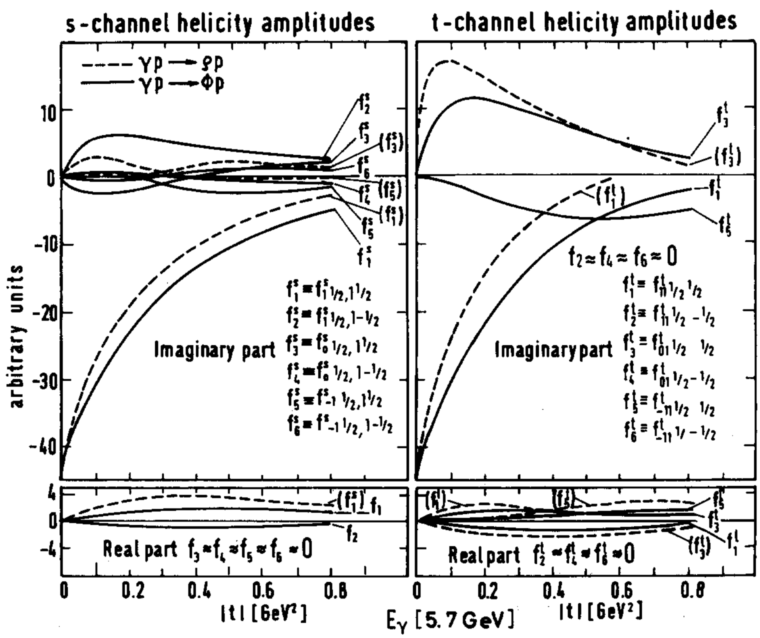

Fig. 20. The t dependence of the helicity amplitudes computed for diffractive ϕ photoproduction are drawn as solid lines. For comparison, the helicity amplitudes for the ρ^0 photoproduction are shown by the dashed curves.

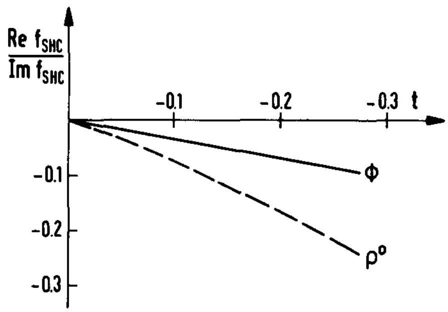

Fig. 21. Real to imaginary ratio of the (SHC) amplitude as computed in sect. 6.

and t-channels are plotted in fig. 20. For a comparison, the corresponding helicity amplitudes for ρ^0 photoproduction obtained by Derado et al. * are shown as broken lines after being normalized to the scale of the ϕ photoproduction amplitudes.

One notices that the imaginary part of the s-channel helicity conserving amplitude $f_1 \equiv f_{1\ 1/2\ 1\ 1/2}$ is the most dominant one. There are however also small contributions from s-channel helicity non-conserving amplitudes. This model yields also an information on the ratio of the real to imaginary part η of the SHC amplitudes f_1 : η is substantially smaller in phi photoproduction as compared to rho photoproduction in the entire t-range considered (see fig. 21).

7. Spin-parity structure of the KK system outside of the Φ

The angular momentum structure of the K^+K^- system has been studied also outside of the ϕ mass by analyzing the K^+ angular distribution in the K^+K^- helicity frame as a function of the K^+K^- invariant mass. The most notable feature is a dramatic change of the K^+K^- angular distribution when one passes over the ϕ mass region (see fig. 17). The $\sin^2\theta_H$ distribution in the ϕ region changes abruptly in character going to larger KK masses, exhibiting a distribution which has predominantly a $\cos^2\theta_H$ dependence. Taking a $t - t_{min}$ range from 0 to 0.20 GeV^2 and mass bins ΔM_{KK} = 0.01 GeV, we computed moments of spherical harmonics of the M_{KK} angular distribution in the helicity frame using the relation

$$\langle Y_L^M \rangle = \sum_i W_i(\theta_i^H, \phi_i^H, M_{KK})\, Y_L^H(\theta_i^H, \phi_i^H)\,. \tag{7.1}$$

W_i is the acceptance corrected event rate in the angular and mass bin considered.

For each mass bin the acceptance weights have been evaluated using Monte Carlo technics. In fig. 22 we plotted the normalized moments $\langle Y_L^M \rangle / \langle Y_0^0 \rangle$ as a function

* The authors of ref. [16] used the value 0.5 GeV^{-2} for the slope of the pomeron trajectory.

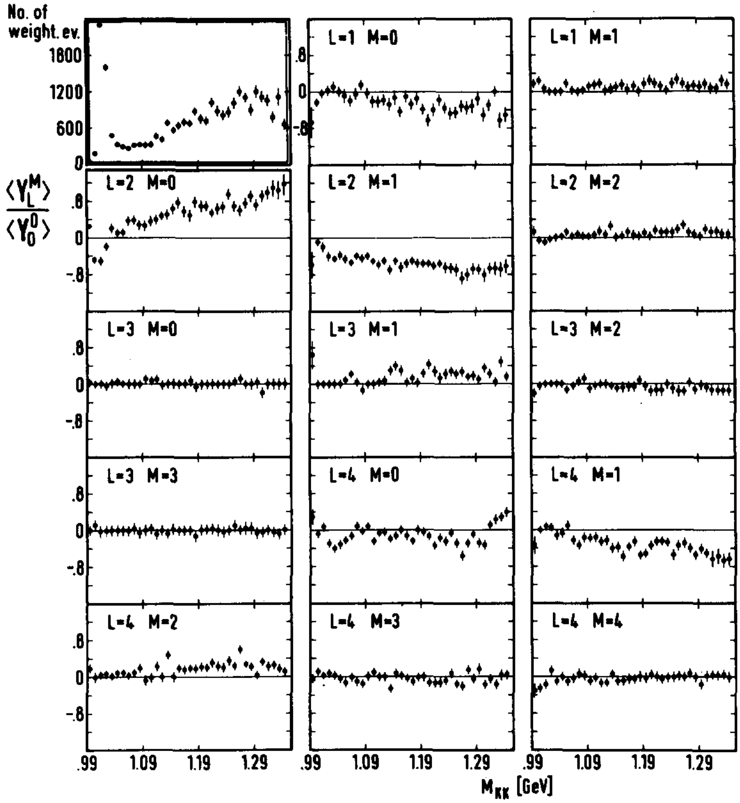

Fig. 22. Normalized moments of spherical harmonics of the K^+K^- decay distribution in the helicity system as a function of the K^+K^- invariant mass.

of M_{KK}. The spectra of the moments above the ϕ exhibit in general a very smooth dependence on the KK mass, which is an indication that the number of amplitudes contributing there to the KK final state is not large.

The moment for $L = 2, M = 0$, representing the helicity conserving part of the spin-1 amplitude, shows a negative bump at the ϕ mass. It crosses the zero line already at $M_{KK} = 1.05$ GeV increasing almost smoothly to large positive values. Small wiggles also in higher moments between $M_{KK} = 1.06$ GeV and $M_{KK} = 1.1$ GeV might indicate the presence of interfering resonant partial waves. The odd-integer moments are practically always zero. A small signal of $\langle Y_1^0 \rangle$ below the ϕ mass which disappears at the ϕ mass can be interpreted as an interference between the helicity non-conserving part of the ϕ production and the presence of the $S_{993}(0^+)$ meson. Although the KK mass distribution shows no direct evidence of the presence of S_{993}, the clear interference signal was the basis for an analysis to estimate limits for the photoproduction cross section of the $S_{993} \to K^+K^-$. Assuming the width and mass reported in the Table of Particle Properties we estimate an upper limit for the cross section of this reaction:

$$\sigma(\gamma p \to pS_{993} \to pK^+K^-) \leqslant 2.7 \pm 1.5 \text{ nb} .$$

From the amplitude analysis we obtained the result that the assumption of a real amplitude for the production of a resonant state at $M_{KK} = 993$ MeV is well consistent with the data. For details of the analysis and results see ref. [20].

8. The inelastic ϕ production

By eliminating events due to reaction (1.1) a substantial sample $\phi \to K^+K^-$ events remained, which failed to fit the elastic hypothesis $\gamma + p \to K^+ + K^- + p$. Hence the remaining events are of the inelastic type

$$\gamma + p \to \phi + X \to K^+ + K^- + X , \qquad (8.1)$$

where X denotes a missing mass different from the proton mass.
The evaluation of the differential cross section of the inelastic reaction with respect to both, the missing mass M_x and $t - t_{min}$, needed a careful study of the acceptance corrections of the experimental apparatus, and of the background subtraction under the ϕ. In the Monte Carlo calculation of the effective detection efficiency for reaction (8.1) the following effects have been taken into account, in addition to the effects already considered for the elastic data, and were used as corrections in the off-line analysis.

(i) The momenta of the decay kaons are for kinematic reasons lower than in the case of elastic data. Thus the decay in flight corrections are of greater importance, in particular because muons from K-decay can cause a veto signal in the Čerenkov coun ter.

(ii) Fast pions from the bulk of the inelastic final states can in general hit the Čerenkov counter and generate an antisignal.

(iii) The front counter (F) will frequently be triggered by inelastic final state particles. This effectively constitutes an enlarged trigger acceptance for inelastic data.

(iv) Multiprong events, not recognized or considered in the analysis procedure, may contribute to reaction (8.1).

The inelastic sample has been selected by cutting the distribution of the invariant K^+K^- mass M_{KK} around the ϕ mass region, $1.01 \leqslant 1.03$ GeV and demanding the missing mass $M_X \geqslant 1.20$ GeV. The events were taken from an energy range 4.6 GeV $\leqslant E_\gamma \leqslant 6.7$ GeV. This mass cut is equivalent within our uncertainties to a selection on the basis of a kinematic one-constraint fit if we demand that the fit probability for the elastic hypothesis is smaller than 0.001, see fig. 8. The regions of missing mass and momentum transfer squared are given by $1.20 \leqslant M_X \leqslant 2.10$ GeV and $0 \leqslant |t - t_{min}| \leqslant 0.2$ GeV^2, respectively.

Fig. 23 shows the K^+K^- invariant mass distribution due to reaction (8.1) for 4

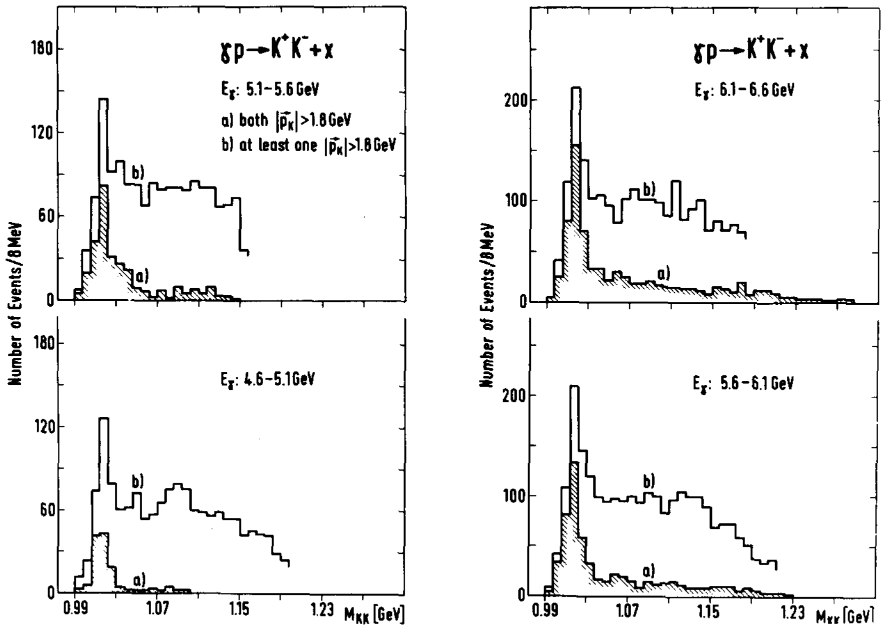

Fig. 23. Invariant K^+K^- mass for $1.2 \leqslant M_X \leqslant 2.1$ GeV in the reaction $\gamma p \to K^+K^-X$ for two experimental cuts (a) and (b).

different energy ranges. The ϕ signal appears on top of a broad K^+K^- background which rises steeply from threshold and becomes rather flat in the mass region above the ϕ. The missing mass M_X corresponding to the ϕ signal was taken from 1.2 to 2.1 GeV.

We applied two different procedures to evaluate the inelastic ϕ cross section: In a cut (a) (fig. 23) we required both K momenta to be larger than 1.8 GeV, thus reducing the background dramatically but not the ϕ peak. In order to compute acceptance weights for this cut assumptions have to be made about the decay angular distribution of inelastically produced ϕ mesons. For cut (b) (fig. 23) the ϕ signal was obtained by fitting in the upper curves a Gaussian and a polynomial to the ϕ signal and the background, respectively.

Both methods may introduce certain biases: cut (a), because the assumption about the angular distribution can influence the acceptance weights; cut (b), because the shape of the background polynomial near threshold determines to some extend the size of the signal. The results obtained by the two methods were in agreement within 20%. The plots and numerical results given in this paper are based on the cut (b). The errors quoted are statistical ones. A systematic uncertainty of about 20% on the cross section can not be excluded.

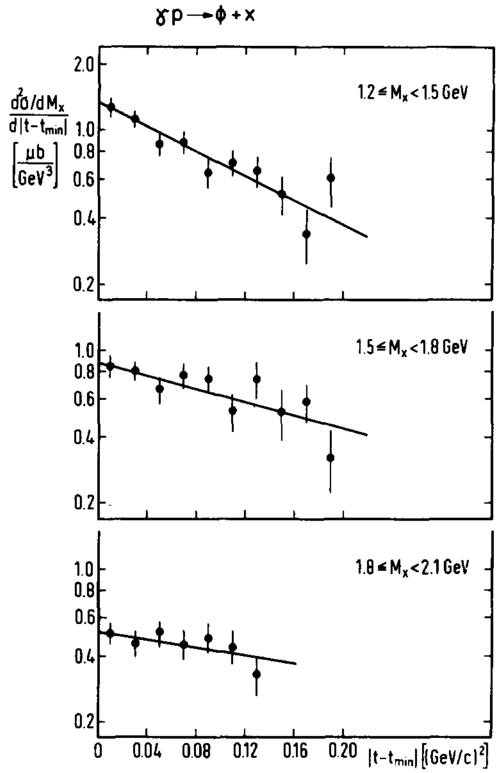

Fig. 24. The double inelastic cross sections $d^2\sigma/dM_X d(t - t_{min})$ as a function of $t - t_{min}$ for different regions in M_X.

Double differential cross sections with respect to $t - t_{min}$ have been evaluated foı 3 mass bins ΔM_X by computing corresponding acceptance weights with Monte Carlo technics (fig. 24).

Differential cross sections integrated over the mass range $1.2 < M_X \leqslant 2.1$ for different γ-energies are plotted in fig. 25 and listed in table 8.

An exponential of the form

$$\frac{d\sigma}{d|t - t_{min}|} = \left.\frac{d\sigma}{dt}\right|_{t=t_{min}} \exp(-B|t - t_{min}|) \tag{8.2}$$

was fitted to the data. Table 8 lists the intercepts $(d\sigma/dt)_{t=t_{min}}$, the slope B, and the signal-over-background ratio for 4 energy bins.

One notices that the inelastic data show in general a flatter t distribution and a relatively large cross section. In particular there is evidence that the slope becomes smaller with increasing M_X. This is shown in fig. 26 where the slope is plotted *versus*

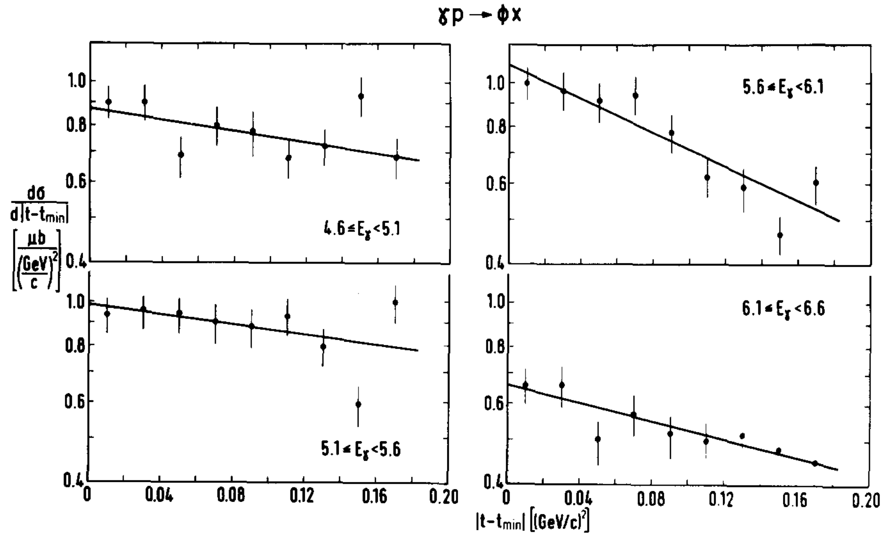

Fig. 25. The inelastic cross section with respect to momentum transfer $t - t_{\mathrm{min}}$ for 4 different energy regions.

Table 8
Table of the inelastic differential cross sections *versus* $t-t_{\mathrm{min}}$ integrated over 1 GeV mass range in μb/GeV^2 for 4 different photon energy regions

$t - t_{\mathrm{min}}$ (GeV^2)	Incident photon energy (GeV)			
	4.6 – 5.1	5.1 – 5.6	5.6 – 6.1	6.1 – 6.6
0.01	0.89 ± 0.09	0.94 ± 0.09	1.00 ± 0.10	0.66 ± 0.06
0.03	0.89 ± 0.09	0.96 ± 0.09	0.96 ± 0.09	0.66 ± 0.06
0.05	0.69 ± 0.07	0.95 ± 0.09	0.92 ± 0.09	0.50 ± 0.05
0.07	0.80 ± 0.08	0.91 ± 0.09	0.94 ± 0.09	0.57 ± 0.05
0.09	0.79 ± 0.08	0.88 ± 0.09	0.78 ± 0.08	0.52 ± 0.05
0.11	0.68 ± 0.07	0.93 ± 0.09	0.62 ± 0.06	0.50 ± 0.05
0.13	0.72 ± 0.07	0.80 ± 0.08	0.59 ± 0.06	0.51 ± 0.05
0.15	0.93 ± 0.09	0.59 ± 0.06	0.47 ± 0.05	0.48 ± 0.05
0.17	0.68 ± 0.07	1.03 ± 0.10	0.60 ± 0.06	0.45 ± 0.04
$\left.\frac{d\sigma}{dt}\right\|_{t=t_{\mathrm{min}}} \left(\frac{\mu b}{\mathrm{GeV}^2}\right)$	0.87 ± 0.07	0.98 ± 0.06	1.1 ± 0.07	0.66 ± 0.10
B(GeV^{-2})	1.47 ± 0.80	1.44 ± 0.70	4.36 ± 0.50	2.29 ± 0.50

The slope values were obtained by assuming a linear exponential form of the t-distribution.

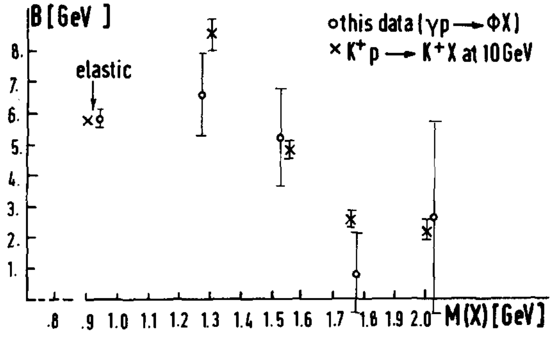

Fig. 26. Slope of the $t - t_{min}$ distribution of the double differential cross section as a function of M_X together with results from the reaction $K^+p \to K^+X$.

M_X together with results from $K^+p \to K^+X$ [21]. For a comparison of elastic and inelastic ϕ production one can consider the ratio of total cross sections

$$\frac{\sigma^{inel}(\gamma p \to \phi X)}{\sigma^{el}(\gamma p \to \phi p)} \qquad X \neq p\,. \tag{8.3}$$

Since due to the limited acceptance of our set up only a part of the total cross sections was recorded and since the t slope for large t values is not known, we have plotted in fig. 27 the ratio

$$\left.\frac{d\sigma^{inel}(\gamma p \to \phi x)}{d|t - t_{min}|} \middle/ \frac{d\sigma^{el}(\gamma p \to \phi p)}{d|t - t_{min}|}\right|_{t=t_{min}}, \tag{8.4}$$

which has been determined in our experiment and carries information related to

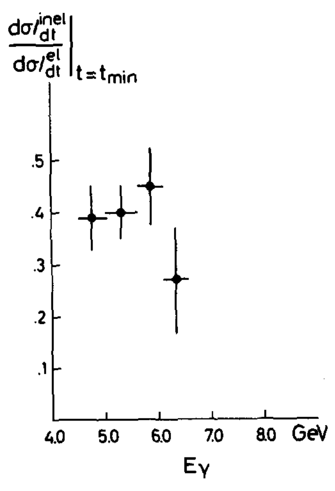

Fig. 27. The ratio of inelastic to elastic differential cross sections at $t = t_{min}$ for different γ energies.

(8.3). The comparatively strong inelastic signal of vector mesons in photoproduction has also been observed in the photoproduction of ρ^0 mesons for photon energies from 4 to 18 GeV [22].

We gratefully acknowledge the support of the synchrotron-operator crew, the floor service and the computing center. We thank Dr. V. Böhmer, Mr. A. Krolzig and his group, our technicians V. Wesche, W. Burmester and A. Höhne and our students W. Hagen, D.F. Jarowoy, K. LeVrang and W. Ziekursch for technical support and assistance. Dr. F.E. Taylor helped us in an early stage of the experiment and designed the tagging system. The Karlsruhe group wishes to express their gratitude to DESY for hospitality and acknowledges the financial support of the Kernforschungs zentrum Karlsruhe and the Bundesministerium für Forschung und Technologie.

References

[1] H.-J. Behrend et al., Phys. Lett. 56B (1975) 408.
[2] (D-BC) ABDHHM, Phys. Rev. 175 (1968) 1669;
(S-CT) R.L. Anderson et al., Phys. Rev. D1 (1970) 21;
D.L. Kreinick, Ph. D. thesis, California Institute of Technology, 1969, unpublished;
(D-MIT) H. Alvensleben et al., Phys. Rev. Lett. 28 (1972) 66;
(C-72) C. Berger et al., Phys. Lett. 39B (1972) 659;
(C-71) G. McClellan et al., Phys. Lett. 26 (1971) 1593;
(S-W) R.L. Anderson et al., Phys. Rev. Lett. 30 (1973) 149;
(S-B-T) J. Ballam et al., Phys. Rev. D7 (1973) 3150;
(BONN) H.J. Besch et al., Nucl. Phys. B70 (1974) 254;
(D-K) This experiment.
[3] H. Joos, Phys. Lett. 24B (1967) 103;
P.G.O. Freund, Nuovo Cim. 48 (1967) 541;
V. Barger and D. Cline, Phys. Rev. Lett. 24 (1970) 1313.
[4] S. Okubo, Phys. Lett. 5 (1963) 165;
G. Zweig, CERN report No. TH. 412 (1964), unpublished;
I. Iizuka, Prog. Theor. Phys. Suppl. 37-38 (1966) 21;
D. Cohren, D.S. Ayres, R. Diebold, S.L. Kammer, A.J. Pawlicki and A.B. Wicklund, Phys. Rev. Lett. 38 (1977) 269.
[5] W. Wentzel et al., Nucl. Phys. 115B (1976) 208.
[6] C. Quigg and E. Rabinovici, Phys. Rev. D13 (1976) 2825.
[7] F.J. Gillman et al., Phys. Lett. 31B (1970) 387.
[8] H. Hirschmann, Kernforschungszentrum Karlsruhe, KFK 2209 (1975).
[9] S. Bartalucci et al., DESY 77/56, 1977.
[10] D. Benaksas et al., Phys. Lett. 39B (1972) 289;
D. Benaksas et al., Phys. Lett. 42B (1972) 507.
[11] D. Joynson and B. Nicolescu, Lab. de Physique Théorique des Particules Elémentaires Université Pierre et Marie Curie Paris, IPNO/TH 75-3;
M. Krammer, Acta Phys. Austriaca 32 (1970) 395.
[12] D.S. Ayres et al., Phys. Rev. D15 (1977) 3105.

[13] W. Koch *in* Analysis of scattering and decay ed. M. Nicolic (Gordon and Breach Science Publishers INC, New York, 1968).
[14] J.D. Jackson, Nuovo Cim. 34 (1964) 1644.
[15] P. Schlamp Ph. D. thesis, Univ. München, 1971.
[16] I. Derado, G. Kronseder, P. Schacht and P. Schlamp, Nucl. Phys. B38 (1972) 541.
[17] L.L. Wang, Phys. Rev. 142 (1966) 1187.
[18] A. Martin, Nucl. Phys. B77 (1974) 226.
[19] D. Heine, Kernforschungszentrum Karlsruhe KFK 2284 (1976).
[20] D.C. Fries et al., Nucl. Phys. B143 (1978) 408.
[21] R.K. Carnegie et al., SLAC-PUB-1610 (1975), unpublished.
[22] A. Silverman, Proc. 1975 Int. Symp. on lepton and photon interactions at high energies, Stanford Univ. 1975, ed. W.T. Kirk.
[23] D.C. Fries, Proc. 6th Recontre de Moriond, Orsay 1971, Ed. I. Tran Thanh Van, 167.
[24] E. Kogan et al., Nucl. Phys. B122 (1977) 383.
[25] D.S. Ayres et al., Phys. Rev. D15 (1977) 3105.